Deformation microstructure of amphibole peridotite from Aheim, Norway and its implication for the seismic anisotropy of the mantle wedge

Sejin Jung[1], Haemyeong Jung[1], and Håkon Austrheim[2]
[1]School of Earth and Environmental Sciences, Seoul National University, Seoul, Korea (shazabi7@snu.ac.kr)
[2]Department of Geoscience, University of Oslo, Oslo, Norway

Abstract Number : EGU2020-4458

1. Introduction

The deformation characteristic of olivine has been the key to understand the mantle flow and the seismic anisotropy of the upper mantle. Fabric transition from A-type to B-type olivine LPO in the mantle wedge was proposed as a possible mechanism for the shear wave splitting pattern change observed from the subduction zone (Jung and Karato, 2001; Jung et al., 2006). The Western Gneiss Region, Norway had undergone UHP metamorphism and subsequent retrogression associated with the Scandian Orogeny (Kostenko et al., 2002; Brueckner et al., 2010). The microstructures of amphibole peridotites from the Åheim, Norway were studied to understand the evolution of microstructures of olivine through the Scandian Orogeny and the subsequent exhumation process. The LPO of olivine and amphibole in the Åheim amphibole peridotite were analyzed to study the olivine fabric transition observed from the naturally deformed peridotite and its implication for the seismic anisotropy of the subduction zone.

2. Previous study

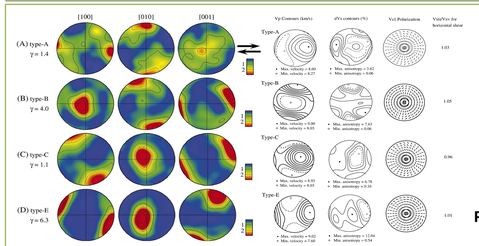

Figure 1. Pole figure and seismic anisotropy of various types of olivine LPO (Jung & Karato, 2001; Katayama et al., 2004; Jung et al., 2006)

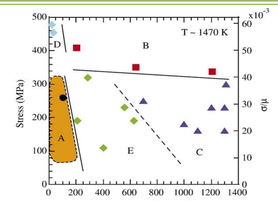

Figure 2. A fabric diagram of olivine at P = 0.3 - 2 GPa, T = 1470 – 1570 K showing the dominant fabric as a function of stress and water content (Jung & Karato, 2001; Katayama et al., 2004; Jung et al., 2006)

Experimental study at high pressure & temperature showed that LPO of olivine can be classified into 4 types; A-type, B-type, C-type, and E-type LPO of olivine (Jung & Karato, 2001; Katayama et al., 2004; Jung et al., 2006). Examples of each type of olivine and seismic anisotropy calculated from the LPO of olivine are shown in **Fig. 1** and fabric diagram of olivine showing the dominant fabric as a function of stress and water content is illustrated in **Fig. 2**.

3. Geological setting

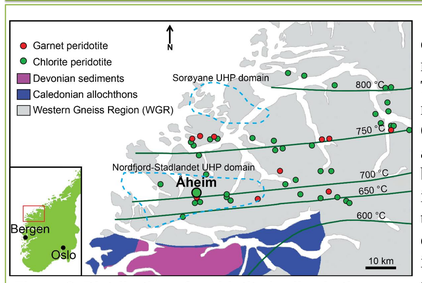

Figure 3. Distribution of peridotite bodies in the WGR, Norway.

The WGR in the western Norway is mostly composed of orthogneisses and paragneisses with many peridotite or eclogite bodies emplaced (**Fig. 3**). The Proterozoic protolith had undergone UHP metamorphism associated with the Scandian Orogenic event from 425 to 400 Ma (Austrheim et al., 2003; Hacker, 2010). The orogenic peridotite bodies in the Nordfjord–Stadlandet UHP domains include peridotite bodies which were trapped during the uplift stage (Brueckner et al., 2010). In the course of exhumation process, peridotites were infiltrated by aqueous fluids and retrograded to the chlorite peridotite (Kostenko et al., 2002; Brueckner et al., 2010).

4. Experimental method

Figure 4. SEM with EBSD system at SNU

Figure 5. Nicolet 6700 FTIR spectrometer and continuum IR microscope at SNU

EBSD analysis

LPO was determined using electron backscattered diffraction (EBSD) in SEM. We used JEOL JSM-6380 scanning electron microscope (SEM) (**Fig. 4**) housed at the School of Earth and Environmental Sciences (SEES) in the Seoul National University (SNU). For EBSD anaylsis, we used HKL system with Channel 5 software. Seismic velocity and anisotropy of the Åheim amphibole peridotite sample was calculated by ANIS2k and VpG programs (Mainprice, 1990) on the basis of the LPO data.

FTIR analysis

Water content of olivine in the samples was measured using Fourier transformation infrared (FTIR) spectroscopy. For FTIR device, we used Nicolet 6700 from Thermo Electron Corporation (**Fig. 5**). Water content of olivine was calculated using the FTIR result. The water content of olivine was calculated using the calibration method described by Paterson (1982). To identify the component of the inclusions in the olivine, additional FTIR analysis was performed for the olivines with inclusions.

5. Result: texture

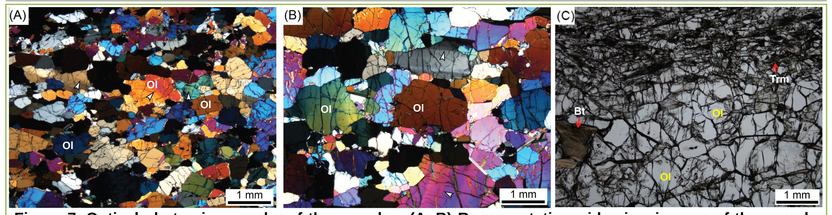

Figure 7. Optical photomicrographs of the samples. (A, B) Representative wide view images of the sample 446 (A) and the sample 448 (B). White arrows indicate the subgrain boundaries. (C) Tremolite-rich layer observed from the sample 443. Ol: olivine, Trm: tremolite, Bt: biotite.

The Åheim amphibole peridotite samples have a porphyroclastic texture and contain primarily olivine (>90%) with minor amount of amphibole, chlorite, opx, biotite, and spinel. Olivine grains are well elongated along the foliation plane. Undulose extinction and subgrain boundaries were very frequently observed from both samples (**Fig. 7A, B**). Tremolite-rich layer with about 50 % modal composition of tremolite is observed from the sample 443 (**Fig. 7C**).

6. Result: EBSD analysis

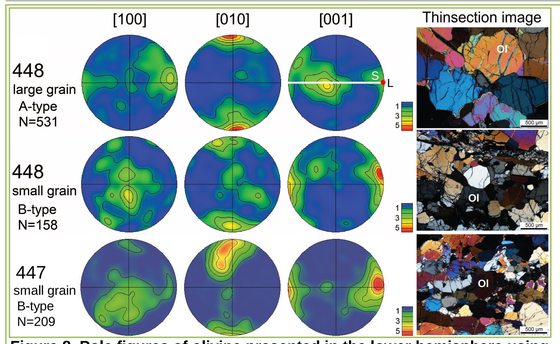

Figure 8. Pole figures of olivine presented in the lower hemisphere using an equal-area projection obtained from large grains including the porphyroclasts and recrystallized small grains of the sample 448 and 447. The white line (S) shows foliation and the red dot (L) shows lineation.

Detailed EBSD analysis of the Åheim amphibole peridotite showed that the LPO of olivine changed depending on the structure and mineral assemblage of the sample. For the sample 447 and 448, the olivine LPO observed from the coarse grains including porphyroclasts (448 large grain) was A-type (**Fig. 8**), but the olivine LPO observed from the recrystallized fine grains (447, 448 small grain) was B-type (**Fig. 8**).

In case of sample 443, the LPO of olivine obtained from the tremolite-poor layer (443 Trm-poor) was A-type, but the LPO of olivine obtained from the tremolite-rich layer (443 Trm-rich) was B-type (**Fig. 9**). Tremolite in the tremolite-rich layer showed the Type-III LPO of amphibole (Ko & Jung, 2015; **Fig. 9**).

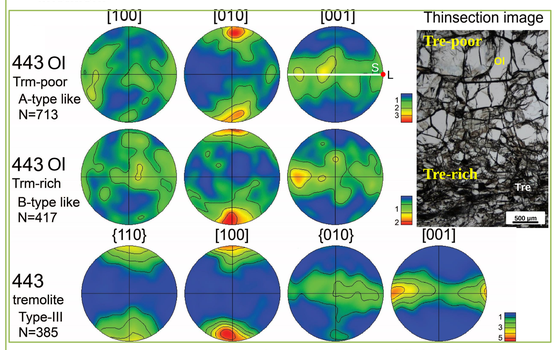

Figure 9. Pole figures of olivine and tremolite presented in the lower hemisphere using an equal-area projection obtained from tremolite-rich layer and tremolite-poor layer of the sample 443. The white line (S) shows foliation and the red dot (L) shows lineation.

The result was recently published (Jung et al., 2020).

7. Result: FTIR analysis

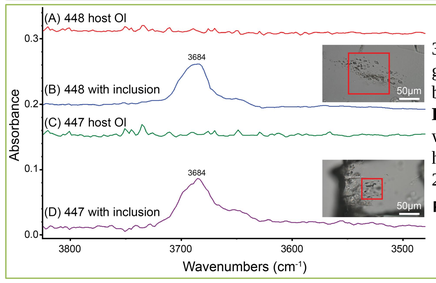

Figure 10. Unpolarized FTIR spectra of olivine and optical photomicrographs of olivine in transmitted light where hydrous inclusions are found.

Average water content of all samples was about 320 ± 30 ppm H/Si. FTIR analyses on the olivine grains with inclusions showed strong absorption bands in the range 3,400 to 3,750 cm^{-1} (**Fig. 10B, D**). IR peaks were found at 3,688, 3648, 3630 cm^{-1}, which indicates the presence of serpentine as hydrous inclusion inside olivine (Khisina et al., 2001; Miller et al., 1987).

8. Result: dislocation microstructure in TEM

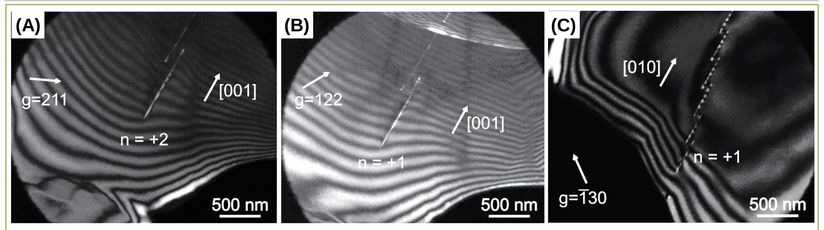

Figure 10. Representative weak-beam dark-field images showing dislocation microstructure of olivine in the sample 447 (A, B) and 448 (C). The diffraction vectors are noted in each image as g and the white arrow, and n value indicate the number of the terminating thickness fringes for each image.

The thickness-fringe method (Ishida et al., 1980; Miyajima and Walte, 2009) was applied in weak-beam dark-field (WBDF) TEM image to identify the Burgers vector and the slip system of disloctions observed from the olivine. Dominant slip system of free dislocations observed from the olivine was (010)[100] (**Fig. 10A, B**). (010)[001] and (001)[100] dislocations were also observed as minor dislocation slip systems. Subgrain boundary which consist of (001)[100] dislocations was observed during TEM observation on the sample 448 (**Fig. 11 C**).

9. Implications for seismic anisotropy

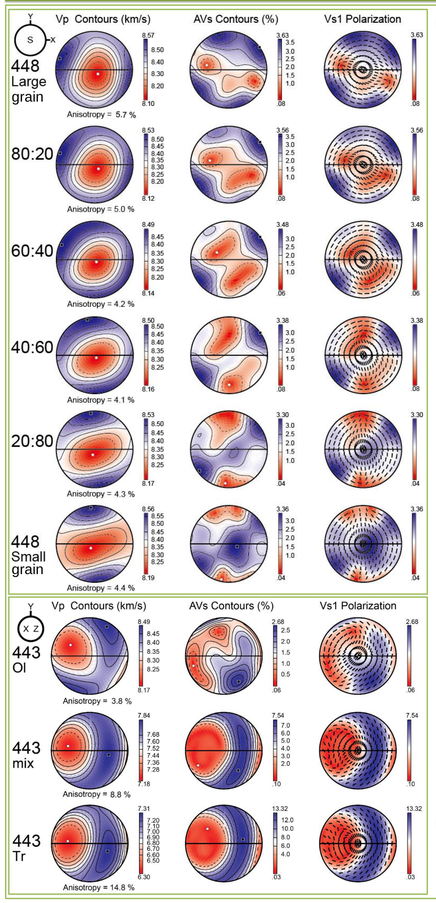

Figure. 11. Effect of degree of recrystallization of olivine on seismic velocity and anisotropy. LPO data of olivine from 448 large grain and 448 small grain (Fig. 8) was mixed with 6 different mixing ratio; 100:0, 80:20, 40:60, 60:40, 20:80, and 0:100.

Seismic velocity and anisotropy of the Åheim amphibole peridotite were calculated to estimate an effect of degree of recrystallization of olivine on the seismic anisotropy. The LPO of the sample 448 was chosen for the original raw data because of its clear porpyroclastic texture and fabric transition from A- to B-type olivine LPO (**Fig. 7B, 8**). Calculated seismic velocity and anisotropy are illustrated in **Fig. 11**. In case of the 448 large grain, a polarization direction of the fast shear wave is subparallel to the flow direction. With the increasing ratio of the sample 448 small grain, the polarization direction of the fast shear wave started tilting and became subnormal to the flow direction around 40:60 ratio. This result indicates that with the 60 % of recrystallization rate, a trench parallel shear wave splitting is expected from the mantle wedge.

In addition, the LPO of the olivine and tremolite in the tremolite-rich layer of sample 443 (**Fig. 9**) were chosen to estimate the influence of the amphibole in the seismic anisotropy of the mantle wedge. With a dipping angle of 45°, the polarization direction of the fast shear wave was oblique to the lineation direction when only the olivine LPO of sample 443 was considered (**Fig. 12**). However, the polarization direction of the fast shear wave was subnormal to the lineation direction when the amphibole LPO was mixed with the olivine LPO of sample 443 (**Fig. 12**).

Figure. 12. Effect of amphibole on seismic velocity and anisotropy. LPO data of olivine and amphibole from 443 tremolite-rich layer (Fig. 7C, 9) was mixed with the ratio of 40:60.

References

Austrheim, H. et al., 2003. Precambrian Research 120, 149-175.
Brueckner, H.K. et al., 2010. Lithos 117, 1-19.
Hacker, B.R., 2010. Tectonophysics 480, 149
Ishida, Y. et al., 1980. Philos. Mag. A-Phys. Condens. Matter Struct. Defect Mech. Prop. 42, 453-462.
Jung, H. and Karato, S., 2001. Science 293, 1460-1463.
Jung, H. et al., 2006. Tectonophysics 421, 1-22.
Jung, H. et al., 2009. Nature Geoscience 2, 73-77.
Jung, S. et al., 2020. Minerals 10(4), 345.
Katayama, I. et al., 2004. Geology 32, 1045-1048.
Karato, S., 1987. Phys. Chem. Minerals 14, 245-248.
Kostenko, O. et al., 2002. Geofluids 2, 203-215.
Ko, B. and Jung, H., 2015. Nat. Commun. 6, 10.
Mainprice, D., 1990. Computers & Geosciences 16, 385-393.
Miller, G.H. et al., 1987. Physics and Chemistry of Minerals 14, 461-472.
Miyajima, N. and Walte, N., 2009. Ultramicroscopy 109, 683-692.
Paterson, M. S., 1982. Bulletin De Mineralogie 105, 20-29.